Renewable Energy 255 (2025) 123707

Contents lists available at ScienceDirect

Renewable Energy

journal homepage: www.elsevier.com/locate/renene

Wave interference and energy conversion in a 3D land-fixed oscillating water column system

Heath Palmer [a],*, Ming Zhao [a], Helen Wu [a], Pan Hu [a], Adnan Munir [a], Zhang Qin [b],*, Vatsal Dhamelia [a]

[a] *Western Sydney University, School of Engineering, Design and Built Environment, Penrith, 2751, NSW, Australia*
[b] *Ocean University of China, Qingdao, Shinan District, Shandong, China*

ARTICLE INFO

Keywords:
Wave interference dynamics
Flume resonance effects

ABSTRACT

This study examines how flume width affects the performance of a land-fixed Oscillating Water Column (OWC) wave energy converter by analysing wave interference and its link to efficiency. While wave interactions in confined flumes are known to impact device performance, the effect of the width-to-wavelength ratio (W/L) has not been fully characterised. A validated numerical model incorporating second-order Stokes waves and Shear Stress Transport (SST) $k-\omega$ turbulence modelling was used to simulate flume widths ranging from 2 to 4.5 wavelengths. Reflected and scattered wave components were isolated to evaluate their influence on local wave dynamics and OWC efficiency. Results show that integer W/L ratios (e.g., $W/L = n$) generate constructive interference, enhanced energy transmission, and higher OWC efficiency. Non-integer ratios (e.g., $W/L = n + 1/2$) disrupt transverse resonance, leading to increased cancellation and reduced performance. A novel interference metric is introduced to quantify the reflected/scattered contribution and its correlation with efficiency. These findings offer guidance for OWC spacing in nearshore arrays, where aligning devices with constructive interference zones may improve overall energy capture.

1. Introduction

Oscillating water columns (OWCs) represent a promising technology for harnessing wave energy, providing a sustainable means of electricity generation in coastal environments. The efficiency of an OWC is strongly influenced by the interaction between incident waves and the structure, with wave interference, resonance, and energy distribution within the flume playing pivotal roles. Optimising these interactions is essential to improve the performance of OWCs and advance their commercial viability.

The study of Oscillating Water Columns (OWCs) has advanced significantly, with extensive research into optimising design and understanding wave interactions to improve energy conversion efficiency. Hydrodynamic performance has been investigated under varying conditions, focusing on structural and geometric parameters. Wang and Zhang [1] explored the performance of dual-chamber OWCs in wave flumes, demonstrating the influence of flume width and sidewall effects on energy capture. They showed that while sidewall effects in narrow flumes could lead to overestimated efficiencies, careful design adjustments, such as integrating harbour walls, could enhance energy extraction. Similarly, Muduli et al. [2] analysed pile-restrained U-shaped OWCs, identifying inward-inclined walls as the most effective for energy conversion, despite the construction challenges associated with this design.

Geometric optimisation has also been a key area of focus. Razavi et al. [3] utilised OpenFOAM and genetic algorithms to optimise OWC designs under sloshing conditions, revealing that adjustments to inlet height and angle significantly enhanced system performance. Likewise, Peymani et al. [4] investigated I-beam attenuator OWCs, highlighting how chamber length and skirt height modifications influenced wave quality and efficiency. These findings underscore the critical role of geometric design in enhancing energy conversion. In long-wave conditions, Xu et al. [5] demonstrated that U-shaped OWCs outperformed conventional designs by reducing sloshing and improving efficiency, with viscous losses in the U-duct identified as a critical factor requiring optimisation.

The importance of 3D effects and resonance has been highlighted in experimental and numerical studies. Sun et al. [6] showed that 3D effects near resonance enhance efficiency, with performance exceeding unity under optimal conditions. Similarly, Didier and Teixeira [7] analysed arrays of OWCs integrated into convergent breakwater designs, revealing improved energy capture under optimal wave periods

---

* Corresponding authors.
E-mail addresses: Heath.Palmer@westernsydney.edu.au (H. Palmer), zhangqin2000@ouc.edu.cn (Z. Qin).

https://doi.org/10.1016/j.renene.2025.123707
Received 26 February 2025; Received in revised form 10 May 2025; Accepted 7 June 2025

and device spacing. Additionally, Medina Rodríguez et al. [8] used a Boundary Element Method to investigate land-fixed OWCs, illustrating how chamber geometry and air compressibility influence capture width and resonance frequencies.

While these studies have deepened our understanding of OWC performance, there remains a gap in linking the spatial distribution of wave energy and interference intensity to practical design considerations for OWCs. Previous work has often focused on structural or geometric optimisation without fully exploring the role of wave interference.

Wave separation techniques have established a critical foundation for analysing wave interactions, with significant contributions from several studies. Goda and Suzuki [9] introduced a Fourier-based technique to separate incident and reflected/scattered waves in both regular and irregular wave systems. Their method, which used wave amplitudes derived from two adjacent gauges, proved effective in estimating reflection coefficients and highlighted the importance of optimal gauge placement to minimise errors. While challenges remained with nonlinear effects and boundary interactions, the study provided a reliable framework for analysing wave dynamics.

Building on this foundation, Zhu [10] developed the Transfer Function Method (TFM), a novel approach for separating incident and reflected/scattered waves in regular wave systems, validated through numerical and physical experiments. Subsequently, Suh et al. [11] applied a least-squares approach to separate incident and reflected/scattered waves in wave–current flumes, extending the analysis to regular and irregular waves. Lin and Huang [12] advanced this field by developing a method to decompose incident and reflected/scattered higher harmonic waves using four wave gauges, successfully validated through physical wave flume experiments. This study demonstrated the ability to accurately capture harmonic interactions, even in nonlinear wave systems.

Further advancements were made by Eldrup and Andersen [13], who extended wave separation methods to highly nonlinear, two-dimensional irregular wave fields. Incorporating second-order wave theory and amplitude dispersion corrections, their approach effectively separated bound and free wave components, with validation against numerical and physical experiments. This work addressed challenges such as shoaling and wave complexity, offering improved accuracy in nonlinear conditions, albeit at the cost of significant computational resources.

More recently, Herdayanditya et al. [14] explored spatial uniformity in numerical wave tanks under various boundary conditions, evaluating Regular Sommerfeld, Generalised Sommerfeld, and Relaxation Zone approaches. Their findings demonstrated that Relaxation Zones provided the lowest reflection coefficients and the most uniform wave fields, effectively suppressing reflections even for nonlinear waves. This highlighted the critical role of boundary condition selection in minimising wave reflections and ensuring accurate wave field simulations.

Despite these advancements, such methodologies have not yet been applied to analysing Oscillating Water Column (OWC) efficiency, particularly concerning the spatial distribution of wave interference and its effect on energy capture. Complementing these studies, Wei et al. [15] investigated wave re-reflection and its impact on the performance of an Oscillating Wave Surge Converter (OWSC). Re-reflected/scattered waves from the flume's wave-maker were shown to alter the incident wave field, affecting wave profiles, flap motion, and slamming forces. These re-reflection effects introduced discrepancies between experimental and numerical results, underscoring the need for reflection mitigation strategies, such as active absorption systems, to enhance experimental accuracy and better replicate real-world conditions.

The study examines the influence of flume width, which conceptually represents the spacing between neighbouring OWCs along a coastline. In such configurations, waves typically approach the shore at near-normal incidence due to bathymetric refraction, and oblique wave directions are not commonly encountered. Oblique wave incidence is more relevant in offshore breakwater or floating OWC arrays, where varying wave directions are expected [16,17]. For this reason, the current analysis is restricted to normal wave incidence. Specifically, the analysis focuses on wave fields' amplitude and phase behaviour, wave interaction dynamics, and energy distribution across a range of integer and non-integer width ratios. By isolating the reflected/scattered wave components, the study characterises how wave reflections and transverse resonance conditions influence OWC efficiency. Fig. 1 illustrates the computational domain and OWC device, a representative model for evaluating wave interactions in a broader row of OWCs. The findings emphasise the role of OWC spacing in shaping resonance conditions and energy capture efficiency. This study provides insights to optimise wave energy system design by examining wave interaction mechanisms.

Table 1
Summary of OWC parameters used for mesh dependency test and 3D geometry numerical validation.

Water depth (h)	0.6 m
Flume width (W)	24.6 m
Incident wave height (H_0)	0.03 m
Total internal chamber width (b)	0.7 m
Total internal chamber depth (W_{OWC})	1 m
Turbine coefficient (K_t)	84 000 Pa m^{-6} s^2
Chamber height (h_c)	0.2 m
OWC wall thickness (C)	0.03 m
Front wall draft (d)	0.12 m
Orifice cross-sectional area (A_T)	0.0047 m^2
Chamber cross-sectional area (A_{OWC})	0.7 m^2

2. Numerical method

The simulations were conducted to evaluate how the flume width influences the performance of the OWC and to investigate the underlying mechanisms. Idealised geometry and regular wave conditions were used to isolate the influence of the non-dimensional width-to-wavelength ratio (W/L). The simulations were based on a single wavelength of L = 3.1415 m, with the flume width (W) varied from $2L$ to $4.5L$ ($W/L = 2$ to $W/L = 4.5$) to examine its effect on wave behaviour and OWC efficiency, with increments of 0.25 wavelengths. The term (W/L) refers to the ratio of the flume width (W) to the wavelength (L) and provides a non-dimensional measure for systematically examining the effect of flume width on wave behaviour and OWC efficiency. The configuration of the computational domain is shown in Fig. 1(a). While the OWC geometry used in this study is consistent with the validation case from Sun et al. [6], the validation case modelled an offshore OWC, whereas the current study focuses on a land-fixed configuration. Here, the OWC protrudes from the sea wall to directly interact with wave dynamics influenced by the flume geometry.

The three-dimensional CFD model from our previous work Zhao et al. [18] is employed in this study to simulate wave motion through OWC devices. The numerical model uses the Arbitrary Lagrangian–Eulerian (ALE) scheme to simulate fluid motion under surface waves by solving the three-dimensional incompressible Reynolds-Averaged Navier–Stokes (RANS) equations coupled with the SST $k-\omega$ turbulence model. The Petrov–Galerkin Finite Element Method (PG-FEM) solves these equations, efficiently handling mesh deformation and ensuring stability across the computational domain. The ALE scheme accommodates fluid domain deformation caused by wave motion, while the SST $k-\omega$ turbulence model provides closure for the RANS equations. To mitigate wave reflection from both the front wall of the OWC device and the sea wall, a damping zone is implemented at the inlet boundary, as shown in Fig. 1(a), with a damping term added to the RANS equations to dissipate fluid velocity.

The RANS equations for a viscous incompressible fluid using the ALE scheme in three dimensions are:

$$\frac{\partial u_i}{\partial x_i} = 0 \tag{1}$$

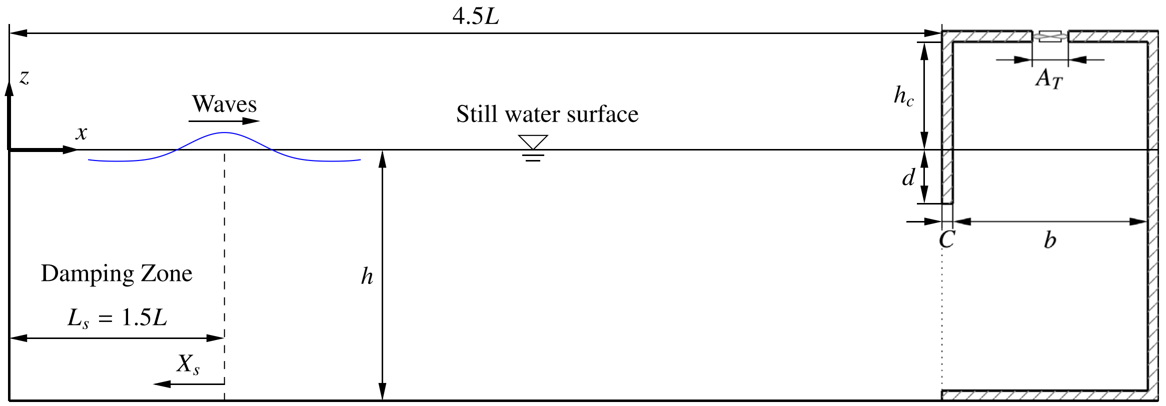

(a) Sectional view of computational domain in zx plane

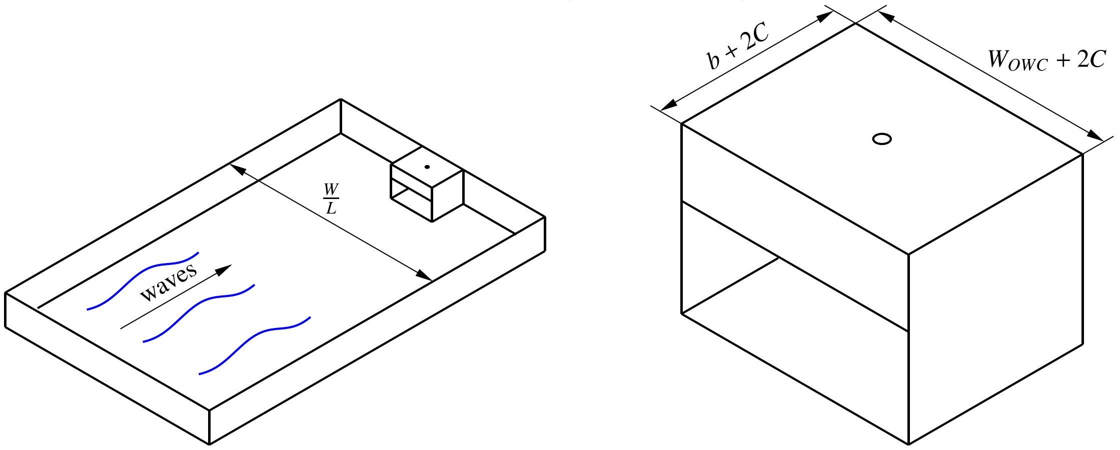

(b) Isometric view of computational domain

(c) Isometric OWC detail

Fig. 1. Overview of the computational domain and geometric configuration used in the study.

$$\frac{\partial u_i}{\partial t} + \left(u_j - u_j^m\right)\frac{\partial u_i}{\partial x_j} = -\frac{1}{\rho}\frac{\partial p}{\partial x_i} + \frac{\partial}{\partial x_j}\left(2\nu S_{ij} - \overline{u_i'u_j'}\right) + g_i - s\left(u_i - u_{i0}\right) \tag{2}$$

where x_1, x_2, and x_3 correspond to the x- (horizontal), y- (transverse), and z- (vertical) directions, respectively. Similarly, $u_1 = u$, $u_2 = v$, and $u_3 = w$ denote the fluid velocity components in the x-, y-, and z-directions. u_j^m is the mesh velocity in the x_j-direction in the ALE scheme. The variables t, p, ρ, ν, and g_i represent time, pressure, water density, kinematic viscosity of water, and gravitational acceleration, respectively.

The strain rate tensor S_{ij} of the mean flow is defined as:

$$S_{ij} = \frac{1}{2}\left(\frac{\partial u_i}{\partial x_j} + \frac{\partial u_j}{\partial x_i}\right) \tag{3}$$

The Reynolds stress term $\overline{u_i'u_j'}$ is modelled as:

$$\overline{u_i'u_j'} = \nu_t\left(\frac{\partial u_i}{\partial x_j} + \frac{\partial u_j}{\partial x_i}\right), \tag{4}$$

where ν_t is the turbulent eddy viscosity.

The damping term $s\left(u_i - u_{i0}\right)$ in (2) absorbs reflected/scattered waves in the damping zone. Here, u_{i0} is the flow velocity of the incident waves, and s is the damping coefficient, defined as in Jacobsen et al. [19] and Zhao et al. [20]:

$$s = \alpha_2 \frac{exp\left[\left(\frac{X_s}{L_s}\right)^{\alpha_1}\right] - 1}{exp\,(1) - 1} \tag{5}$$

The damping zone length L_s is set to 1.5 times the wavelength L, with damping coefficients $\alpha_1 = 1.2$ and $\alpha_2 = 5$.

On the wave surface, the following boundary condition applies:

$$\frac{\partial \eta}{\partial t} + (u - u^m)\frac{\partial \eta}{\partial x_1} + (v - v^m)\frac{\partial \eta}{\partial x_2} + (w - w^m)\frac{\partial \eta}{\partial x_3} = w - s\left(\eta - \eta_0\right) \tag{6}$$

Here, η is the surface elevation, η_0 is the wave surface elevation of the incoming waves, and u, v, w are the fluid velocities in the x_1, x_2, and x_3 directions, respectively. The damping term s absorbs reflected/scattered waves, ensuring accurate boundary behaviour. Pressure on the free surface is atmospheric outside the OWC, while inside the OWC, it is determined by the aerodynamic model, as described in Section 2.1. Boundary conditions for turbulence include zero turbulent energy (k) and zero gradients of the specific dissipation rate (ω) on the free surface. At the inlet, the water flow velocity and wave surface elevation are based on second-order Stokes wave theory.

2.1. Aerodynamic model

An accurate aerodynamic model is essential to predict the air pressure in the OWC chamber, which acts as a pressure boundary condition on the wave surface. The methodology proposed by Josset and Clément [21] forms the basis of the aerodynamic model used in this study, and has been widely applied in other OWC modelling efforts. For instance, Teixeira et al. [22] implemented the same approach to evaluate chamber dynamics, while Gonçalves et al. [23] extended it to large-scale systems. Sheng and Lewis [24] also adopted this formulation in their coupled model of air–water interactions. The model incorporates air compressibility, which has been shown to critically influence energy harvesting in large-scale OWCs. Mia et al. [25] highlighted the importance of compressibility effects in full-scale chambers, while Gonçalves et al. [23] and Sheng and Lewis [24] demonstrated how neglecting these effects can underpredict pressure variations. Viviano et al. [26] further confirmed its impact on energy conversion efficiency through sensitivity analysis.

For the simplified power take-off (PTO) representation used in this study, the quadratic relationship between the air flow rate and the chamber pressure is given by:

$$p_a(t) - p_{a0}(t) = -K_t|Q_t(t)|Q_t(t), \tag{7}$$

where $p_a(t)$ represents the instantaneous air pressure in the chamber, and $p_{a0}(t)$ is the atmospheric pressure. The term $Q_t(t)$ corresponds to the instantaneous air flow rate through the turbine, while K_t is the turbine coefficient that characterises the non-linear relationship between pressure and flow rate.

This quadratic relationship approximates the non-linear behaviour of impulse turbines, which exhibit a stronger dependence of pressure on flow rate compared to linear turbines. While it does not capture the full dynamics of real turbine-generator systems, it enables a consistent comparison of hydrodynamic performance across each configuration considered in this study. More detailed wave-to-wire approaches such as those presented by Ciappi et al. [27,28] and Henriques et al. [29] incorporate turbine geometry, rotational inertia, control strategies, and generator coupling, offering a more complete characterisation of PTO dynamics and energy conversion. However, these models are beyond the intended scope of the present work, which focuses on idealised hydrodynamic resonance under controlled conditions.

The air pressure within the chamber is calculated as:

$$\frac{\dot{p}_a(t)}{p_a(t)} = \gamma \left[\frac{Q_t(t)}{V(t)} \left(1 - \sigma \frac{\rho_a(t) - \rho_{a0}}{\rho_a(t)} \right) - \frac{\dot{V}(t)}{V(t)} \right], \tag{8}$$

The chamber volume change rate is determined by integrating the vertical velocity (v) of the free surface over the chamber cross-sectional area (A_{OWC}):

$$\dot{V}(t) = -\int_{A_{OWC}} v \, \mathrm{d}A_{OWC}, \tag{9}$$

where A_{OWC} represents the chamber cross-sectional area. The relationship between chamber air pressure and density (ρ_a) is assumed to follow an isentropic transformation:

$$p_a \rho_a^{-\gamma}(t) = p_{a0} \rho_{a0}^{-\gamma}, \tag{10}$$

where ρ_a is the instantaneous air density in the chamber, and ρ_{a0} is the atmospheric air density. This relationship allows the air density (ρ_a) to be updated iteratively. The power generated by the turbine is expressed as:

$$P_T(t) = |Q_t(t)[p_a(t) - p_{a0}]|, \tag{11}$$

while the instantaneous non-dimensional power is defined as:

$$P_T^* = \frac{P_T}{P_w}. \tag{12}$$

The hydrodynamic efficiency of the OWC is defined as the ratio of mean turbine power to wave power:

$$\xi = \frac{\bar{P}_T}{P_w}, \tag{13}$$

where $\bar{P}_T$ is the time-averaged turbine power and P_w is the incident wave power, calculated using the second-order Stokes wave theory:

$$P_w = \frac{\rho g H_0^2}{16} \frac{\Omega}{k} \left(1 + \frac{2kh}{\sinh(2kh)} \right) W_{OWC}, \tag{14}$$

where $k = \frac{2\pi}{L}$ is the wave number, $\Omega = \sqrt{gk\tanh(kh)}$ is the angular frequency of the wave, ρ is the water density, g is the gravitational acceleration, and H_0 is the wave height of the incident wave. The wave surface elevation and air pressure are non-dimensionalised as:

$$\eta^* = \frac{2\eta}{H_0}, \tag{15}$$

and

$$P_a^* = \frac{2(p_a - p_{a0})}{\rho g H_0}, \tag{16}$$

respectively.

Table 2
Summary of OWC parameters used for 2D geometry validation.

Water depth (h)	0.8 m
Flume width (W)	0.16 m
Incident wave height (H_0)	0.06 m
Total internal chamber width (b)	0.55 m
Total internal chamber depth (W_{OWC})	0.16 m
Turbine coefficient (K_t)	1 524 475 Pa m^{-6} s^2
Chamber height (h_c)	0.2 m
OWC front wall thickness (C)	0.04 m
Front wall draft (d)	0.14 m
Orifice cross-sectional area (A_T)	0.0028 m^2
Chamber cross-sectional area (A_{OWC})	0.088 m^2

Non-dimensional amplitudes of wave surface elevation, air pressure, and air volume are defined as:

$$A_\eta^* = \frac{\eta_{\max} - \eta_{\min}}{H_0}, \tag{17}$$

$$A_{pa}^* = \frac{p_{a_{\max}} - p_{a_{\min}}}{\rho g H_0}, \tag{18}$$

$$A_V^* = \frac{V_{\max} - V_{\min}}{H_0 A_{OWC}}, \tag{19}$$

where the subscripts max and min represent the maximum and minimum values of the corresponding variable in one wave period.

3. Numerical validation and mesh dependency study

3.1. Numerical validation

To ensure the validity of the model, the numerical results were validated against the experimental studies of the land-fixed Oscillating Water Column (OWC) by Wang et al. [30] and the offshore OWC by Sun et al. [6], using 2D and 3D geometry configurations, respectively. These two studies were selected due to the absence of a suitable experimental dataset for a land-fixed OWC with 3D geometry. The land-fixed study validated the model's accuracy in simulating land-fixed configurations, albeit in 2D, while the offshore study validated the model's accuracy in 3D. The parameters for the 2D numerical validation are given in Table 2, and the geometry used is shown in Fig. 1(a). While the simulation is 3D, there are no 3D effects for 2D geometry, as the flume is only as wide as the OWC opening. The comparison focused on key performance metrics, including efficiency, non-dimensional chamber pressure, and non-dimensional surface elevation. The turbine coefficient K_t was calculated using the method of Brito-Melo et al. [31] for each kh value used in the validation studies, with a value of 1,524,475 Pa m^{-6} s^2 used for the 2D geometry from Wang et al. [30], and an average value of approximately 84,000 Pa m^{-6} s^2 used for the 3D geometry from Sun et al. [6]. Figs. 2(a) and 3 show good agreement between the numerical results of the present study and the experimental data by Wang et al. [30]. The 3D validation geometry is shown in Figs. 5(a) and 5(b), where the flume width is 24.6 m. The OWC geometry used is identical to that used in the mesh dependency test and is given in Table 1. The experimental setup described in Sun's study provided a robust benchmark for evaluating the accuracy of the CFD model.

The comparison of efficiency (Fig. 2(b)), as well as non-dimensional surface elevation and chamber pressure (Fig. 4), between the experimental results of Sun et al. [6] and the numerical results of the present study demonstrates overall good agreement.

3.2. Mesh dependency study

A mesh dependency study was conducted to ensure that the numerical solution is sufficiently accurate, reliable, and independent of the mesh density. Figs. 5(a) and 5(b) present the sketch and isometric

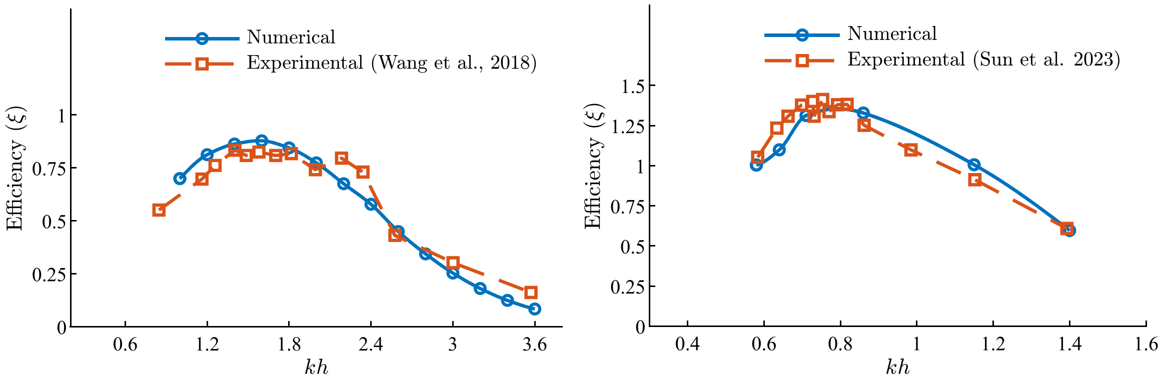

(a) Validation of efficiency against 2D geometry by Wang et al. [30]

(b) Validation of efficiency against 3D geometry by Sun et al. [6]

Fig. 2. Validation of efficiency: present study vs experimental results for 2D and 3D geometries.

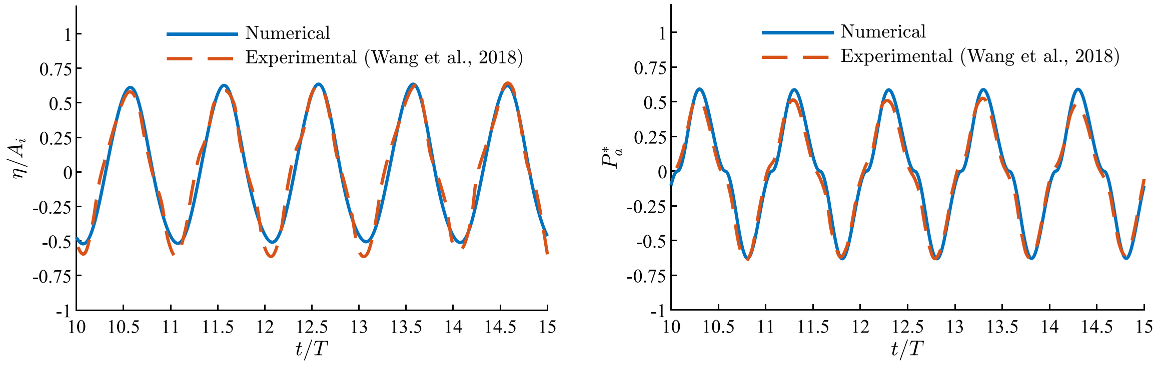

(a) Validation of non-dimensional surface elevation against experimental results using 2D geometry by Wang et al. [30] where T=1.49s

(b) Validation of non-dimensional pressure against experimental results using 2D geometry by Wang et al. [30] where T=1.49s

Fig. 3. Validation of non-dimensional surface elevation and non-dimensional pressure: present study vs experimental results for 2D geometry.

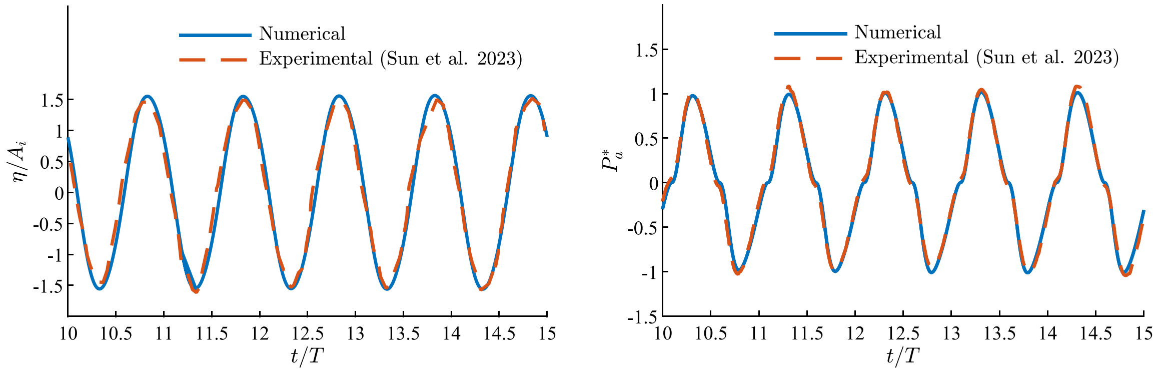

(a) Validation of non-dimensional surface elevation against experimental results using 3D geometry by Sun et al. [6] where T=2.35s

(b) Validation of non-dimensional pressure against experimental results using 3D geometry by Sun et al. [6] where T=2.35s

Fig. 4. Validation of non-dimensional surface elevation and non-dimensional pressure: present study vs experimental results for 3D geometry.

view of the domain configuration used for the study. Simulations were performed at a *kh* of 0.714, which corresponds to the peak *kh* case identified in the study by Sun et al. [6] with the parameters shown in Table 1. The sensitivities of the key output variables, efficiency, pressure, and surface elevation, to variations in mesh density were analysed to identify a configuration that balanced computational efficiency and accuracy, ensuring reliable and feasible results.

To assess the impact of mesh density on the results of the simulation, three mesh densities were considered: coarse, medium, and fine. The OWC chamber wall, with a thickness of 0.03 m, was discretised using 2 elements in the coarse mesh, 4 elements in the medium mesh, and 6 elements in the fine mesh as shown in Table 3 and Fig. 6. The thickness of the first-layer mesh is equal to the element size used to discretise the wall thickness. The medium mesh is shown in Figs. 6(b) and 7, served as the baseline density, with the coarse mesh dividing the OWC chamber wall into half as many elements and the fine mesh using one and a half times as many elements in the incident wave plane (x- and y-axes). The goal was to capture the key physical behaviour of the wave surface and balance computational resource costs while progressively reducing numerical error as the mesh density increased. The total length in the incident wave propagation direction (x-axis) is 47.519 m, with the OWC located at the centre.

Fig. 5(a) illustrates the computational domain, showing the regions of varying mesh density used in the mesh dependency study and

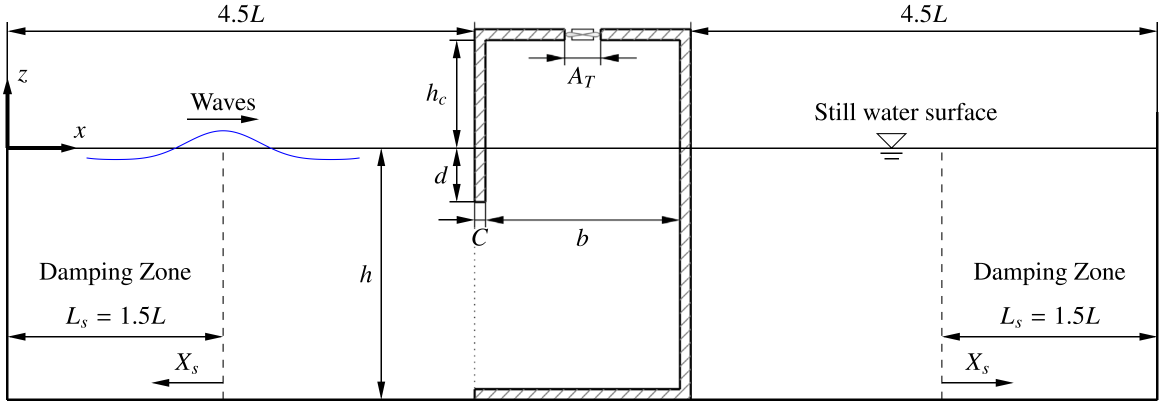

(a) Sketch of computational domain used for mesh dependency study and 3D geometry numerical validation

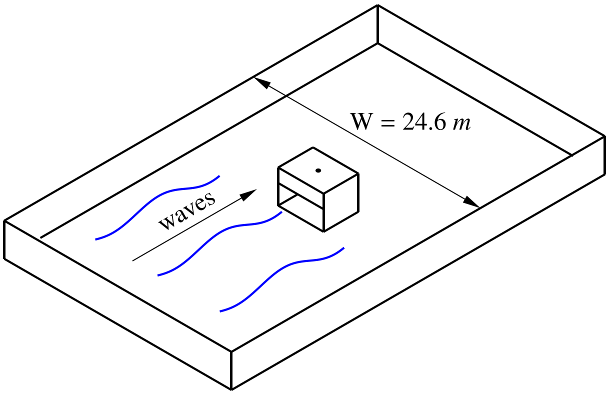

(b) Isometric view of computational domain used for mesh dependency study and 3D geometry numerical validation

Fig. 5. Overview of the computational domain and geometric configuration used for mesh dependency study and 3D geometry numerical validation.

numerical validation. Region A, located immediately around the OWC, is the most refined region, with a first-layer element size of 0.015 m, 0.0075 m, and 0.005 m for the coarse, intermediate, and fine meshes on the OWC wall, respectively. The mesh in this region inflates to $L/20$ for the coarse mesh and $L/40$ for the intermediate and fine meshes. Surrounding Region A is Region B, which has a thickness of half a wavelength ($L/2$) in both the incident wave (x-axis) and transverse (y-axis) directions. In Region B, the mesh density inflates in both the incident and transverse directions (x- and y-axes) from $L/20$ for the coarse mesh and $L/40$ for the intermediate and fine meshes to $L/10$ and $L/20$, respectively.

Region C, located on either side of Region B, extends along the transverse direction (y-axis) and has the same width in the incident wave direction (x-axis) to Region B. The transverse inflation in Region C mirrors that of Region B, but the mesh density in the incident wave direction is non-uniform due to the constraints in the mesh generation process. Beyond Region B in the incident wave direction is Region D, which spans four wavelengths ($4L$) in the incident wave direction and is the same size along the transverse direction (y-axis) as Region B. In Region D, the mesh element sizes are $L/20$ for the coarse mesh and $L/40$ for the intermediate and fine meshes in both the incident and transverse wave directions. Finally, Region E, located at the outer edges of the domain, follows the same inflation pattern as Region C in the transverse direction and adopts the same element sizes as Region D in the incident wave direction.

By systematically increasing the mesh density, the study aimed to identify the point of mesh independence—where further refinement resulted in negligible changes in the simulation results. A smooth transition between regions of different mesh refinement was maintained to avoid numerical artefacts, and particular attention was paid to boundary layer resolution and wave propagation fidelity. The results shown in Fig. 8 of this study show that for instantaneous non-dimensional power (P^*) there is a 8.25% difference between the coarse and medium meshes, but a 0.93% difference between the medium and the fine meshes, and for instantaneous non-dimensional power (P^*) there is a 4.75% difference between the coarse and medium meshes, but a 1% difference between the medium and the fine meshes. This suggests that the medium mesh offers a good balance between accuracy and computational cost.

4. Results and discussion

4.1. Efficiency, pressure, volume, and energy distribution

The simulations of the land-fixed OWC, shown in Fig. 1(a), were conducted using the parameters listed in Table 1. A fixed kh value of $kh = 1.20$ was used, corresponding to a wavelength of $L = 3.1415\,\mathrm{m}$. The flume width varied from $\frac{W}{L} = 2.00$ to 4.50 to investigate the effects of flume width on wave behaviour and OWC performance. The variation in efficiency, non-dimensional pressure amplitude, and non-dimensional volume amplitude with changes in the flume width ratio (W/L), as illustrated in Figs. 9(a) to 9(c), shows local peaks at integer values ($W/L = n$) and local troughs at non-integer values, particularly at $W/L = n + 1/2$, where n is an integer. For all parameters, as the flume width ratio increases, the overall magnitudes decrease for integer values and increase for non-integer values, suggesting that the influence of the width ratio diminishes when the flume becomes sufficiently wide.

These trends are closely tied to the physics of wave resonance and energy distribution within the flume. The flume behaves as a multi-dimensional resonator, supporting both longitudinal and transverse standing waves. The resonance conditions depend on the relationship between the flume dimensions and the wavelength of the incident wave.

Table 3

Summary of mesh parameters for the mesh dependency test.

Parameter	Coarse mesh	Medium mesh (Baseline)	Fine mesh
Elements across the OWC wall thickness	2 elements	4 elements	6 elements
Max element size in the incident wave direction (x-axis)	L/20	L/40	L/40
Total number of elements	413,824	2,330,068	3,013,216
First-layer element size at the wall and wave surface	0.015	0.0075	0.005

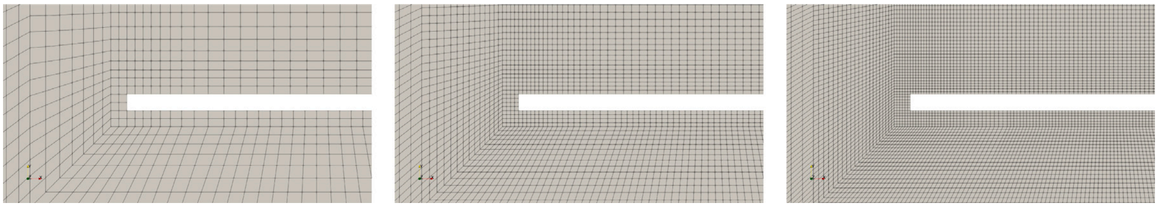

(a) Coarse mesh (2 elements) (b) Medium mesh (4 elements) (c) Fine mesh (6 elements)

Fig. 6. Comparison of mesh density for the OWC chamber wall. The coarse mesh divides the wall into 2 elements, the medium mesh into 4 elements, and the fine mesh into 6 elements.

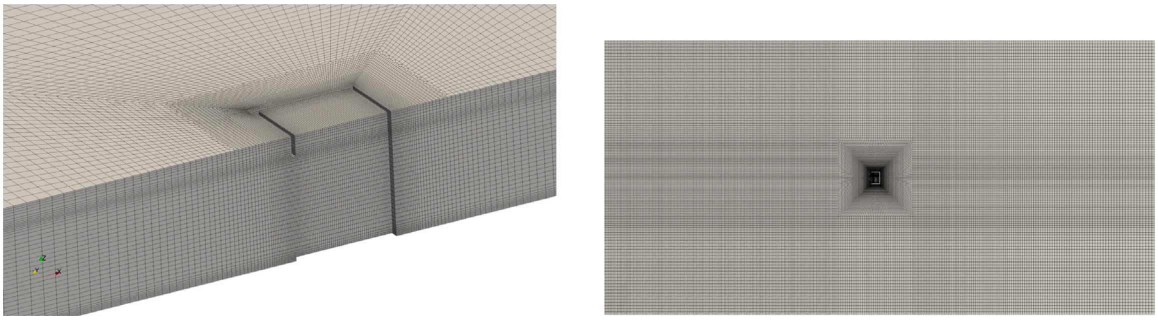

(a) Medium density OWC mesh section. (b) Medium density OWC mesh plan.

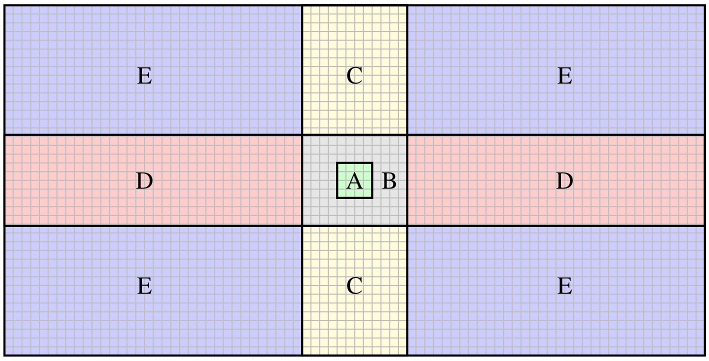

(c) Sketch of computational domain used for mesh dependency study and 3D geometry numerical validation

Fig. 7. Computational mesh layout: cross-section, plan view, and refinement configuration.

Standing waves in the transverse direction form when the flume width (W) satisfies the resonance condition:

$$W = m\frac{L}{2}, \quad m \in \mathbb{Z}^{+},$$

where L is the wavelength of the incident wave and m is the transverse mode number. The fundamental transverse mode occurs at $m = 1$, where the flume width is half a wavelength. Higher mode numbers ($m = 2, 3, \dots$) correspond to wider flume configurations, where multiple transverse wave crests can form across the width. Here, $\mathbb{Z}^{+}$ denotes the set of positive integers. The mode number $m = 1$ represents the fundamental mode (a single half-wavelength across the flume). In contrast, $m \geq 2$ represents higher-order modes with additional nodes and antinodes along the flume width.

Fig. 10 shows the computational domain, highlighting the regions used for analysis, including the near-field region, transverse side regions, and the back wall of the flume. These regions provide a spatial framework for the following discussion, allowing for consistent and precise reference to specific areas within the flume.

Fig. 11 compares the non-dimensional surface wave amplitude between optimal width ratio configurations ($W/L = n$) and non-optimal width ratio configurations ($W/L = n + 1/2$), where $2 \leq n \leq 4$.

For optimal configurations $\frac{W}{L} = n$, as shown in Figs. 11(a), 11(c) and 11(e), the highest wave surface amplitudes are observed on the seaward side of the OWC opening. Additionally, the wave surface elevation is generally smaller and more evenly distributed in the near-field region directly in front of the OWC, along the back wall of the flume, and within the transverse side regions, as shown in Fig. 10. The absence of large wave amplitudes in these areas suggests that the OWC effectively absorbs the wave energy that would otherwise contribute to higher wave heights. Together, these patterns indicate greater energy transmission to the OWC and reduced energy redistribution to other areas of the flume, such as the back and side walls. This further suggests

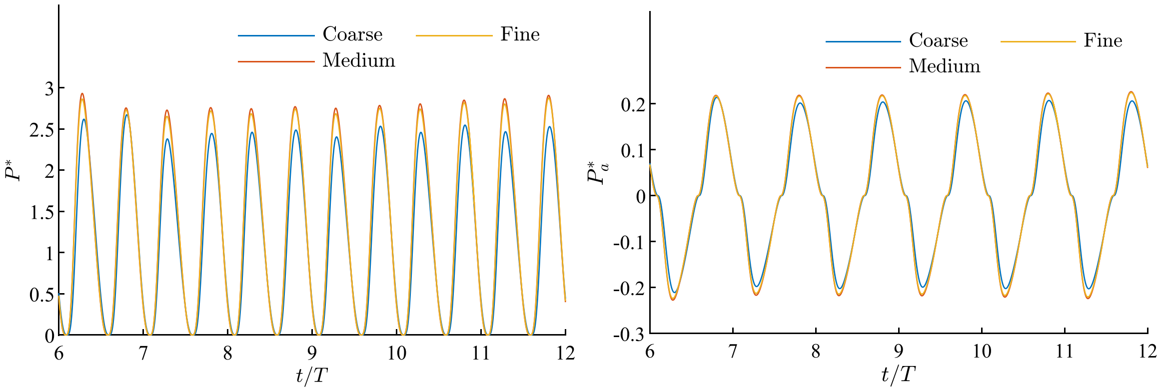

(a)

(b)

Fig. 8. (a) Comparison of instantaneous non-dimensional power, and (b) non-dimensional chamber pressure, for each mesh density considered.

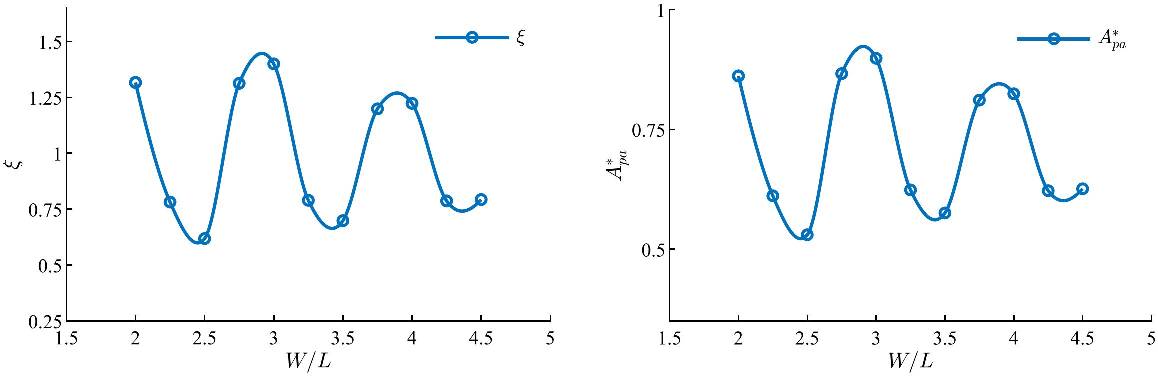

(a) Efficiency for each case considered.

(b) Non-dimensional pressure amplitude for each case considered.

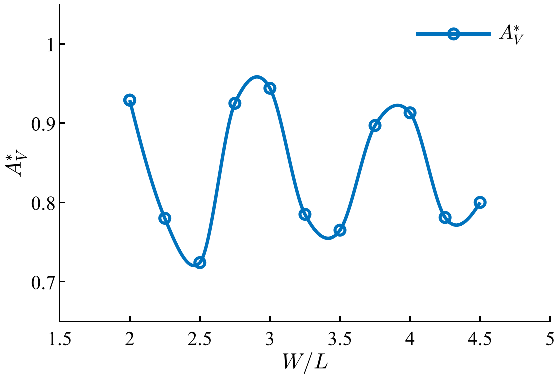

(c) Non-dimensional volume amplitude for each case considered.

Fig. 9. OWC performance metrics including efficiency (a), non-dimensional pressure amplitude (b), and non-dimensional volume amplitude (c) for each configuration considered.

that, for optimal configurations ($\frac{W}{L} = n$), the flume and OWC are likely in a coupled resonant or near-resonant state, where the combination of the flume width and OWC geometry enhances energy absorption and minimises losses.

In contrast, for non-optimal configurations ($W/L = n + 1/2$), the non-dimensional wave height contours, in Figs. 11(b), 11(d) and 11(f) reveal that the highest wave amplitudes in the flume are concentrated on the leeward side of the OWC opening, particularly in the transverse side regions near the side walls of the OWC and the back wall of the flume. In the near-field region, a clearly defined transverse wave pattern emerges, indicating that energy is being redistributed and concentrated in this area rather than contributing to wave-structure interactions in front of the OWC opening. This energy redistribution suggests that the OWC and flume are likely not coupled in a resonant or near-resonant state. As a result, wave-structure interaction is reduced, leading to the observed decrease in efficiency.

Among the non-integer width ratio cases shown in Fig. 12, the $W/L = n + 3/4$ configurations (Figs. 12(b) and 12(d)) exhibit some similarities to the integer width ratio cases, particularly the presence of an antinode or wave height peak directly in front of the OWC opening within the near-field region. This characteristic likely contributes to the observed higher efficiency compared to other non-integer width ratio cases. However, like the $W/L = n + 1/2$ configurations, the waves with the highest amplitudes are concentrated along the back wall, especially at the junctions with the external side walls of the OWC in the transverse side regions. This distribution suggests that the flume and OWC are not in a coupled resonant state, leading to reduced wave-structure interaction, although to a lesser degree than in the ($W/L = n + 1/2$) configurations.

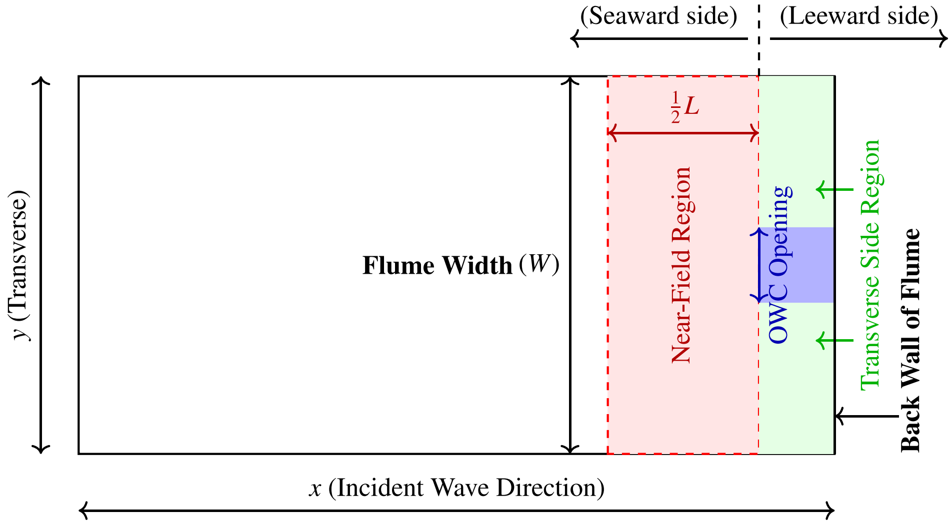

Fig. 10. Plan view of the land-fixed OWC and flume, highlighting the near-field and transverse side regions.

Finally, the $W/L = n + 1/4$ cases (Figs. 12(a), 12(c) and 12(e)) share similarities with other non-integer cases, including high wave amplitudes in the near-field region, transverse side regions, and along the back wall. Although the surface elevation amplitude of the standing wave along the back wall in the $W/L = n+1/4$ cases is smaller than in the $W/L = n+1/2$ and $W/L = n+3/4$ configurations, it has a greater concentration of high wave amplitude peaks on the seaward side of the OWC front opening. This pattern suggests reduced wave-structure interaction, resulting in decreased efficiency.

Resonance effects directly influence the spatial distribution of wave energy within the flume. To better understand the relationship between surface amplitude, energy density, and wave-structure interaction, the wave energy density in the flume is examined in the next section.

4.1.1. Exclusion region and region of analysis

The exclusion region and region of analysis are shown in Fig. 13. The exclusion region consists of the area occupied by the OWC and the portions of the flume that extend beyond the defined analysis region. The region occupied by the OWC was excluded to prevent distortions from localised energy transmission and reflection effects specific to the chamber.

The region of analysis is defined as the area directly in front of the OWC opening, extending laterally across the width of the OWC and spanning a distance of $L/10$ in the $-x$-direction, where L is the wavelength of the incident wave. This selection ensures that the analysis focuses on the immediate wave-structure interaction zone while excluding broader flume effects that could dilute local interference patterns. While similar trends were observed up to approximately $L/4$, the patterns became more diffuse as the region expanded, making $L/10$ the most appropriate choice for clear trend identification and quantitative analysis. The chosen extent balances spatial resolution with physical relevance, capturing the dominant wave dynamics influencing energy conversion efficiency.

4.1.2. Energy density per unit width and its implications

The total energy flux of undisturbed waves (P_w) entering the flume increases with the flume width (W), as the incident wave spans its full width. However, because the same total energy is distributed over a larger domain, the local energy density per unit width remains constant and depends only on the wave properties.

Using the expression for incident wave power from (14), the energy density per unit width is given by:

$$\frac{P_w}{W_{OWC}} = \frac{\rho g H_0^2}{16}\frac{\Omega}{k}\left(1+\frac{2kh}{\sinh(2kh)}\right). \tag{20}$$

This implies that increasing the flume width distributes the same total wave energy over a greater area, reducing the wave energy per unit width and leading to lower wave amplitudes in the domain.

As seen from (21), wave amplitude is proportional to the square root of energy density:

$$A_\eta \propto \sqrt{\text{Energy Density}}. \tag{21}$$

The quadratic dependence between energy density and wave amplitude remains relevant in this study despite the presence of second-order Stokes waves. While nonlinear effects refine the proportionality constant, the fundamental relationship remains unchanged. Given that the waves considered in this study are relatively low amplitude, higher-order contributions are negligible, and the energy density-wave amplitude relationship can be reliably characterised using this principle.

To illustrate the relationship between flume width and wave dynamics, Fig. 14 presents the non-dimensional mean local amplitude of wave surface elevation ($\bar{A}^*_\eta$) for different width ratios. The local mean amplitude of wave surface elevation was calculated as:

$$\bar{A}^*_\eta = \frac{1}{A}\int_A A^*_\eta(x,y)\,\mathrm{d}A \tag{22}$$

where:

- A is the area of the region of analysis,
- $A^*_\eta(x,y)$ is the non-dimensional amplitude of wave surface elevation at each point.

The results demonstrate a clear trend: as the flume width increases, the peaks and troughs in the local mean amplitude of wave surface elevation become less pronounced, indicating a convergence towards a more uniform wave field. This suggests that the influence of flume width on the wave dynamics diminishes as the width increases.

Beyond a certain width, the local mean amplitude of wave surface elevation is expected to stabilise, representing an equilibrium point where further increases in flume width no longer significantly impact the wave dynamics. At this point, the wave patterns are likely governed primarily by the properties of the incident wave rather than the flume geometry.

This trend aligns with the expected reduction in energy density per unit width as the flume becomes wider, distributing the same amount of energy over a larger domain.

Interestingly, the $W/L = n + 3/4$ configurations exhibit higher local mean non-dimensional wave amplitude than the nearest integer-width configurations. However, as seen in the efficiency, pressure, and

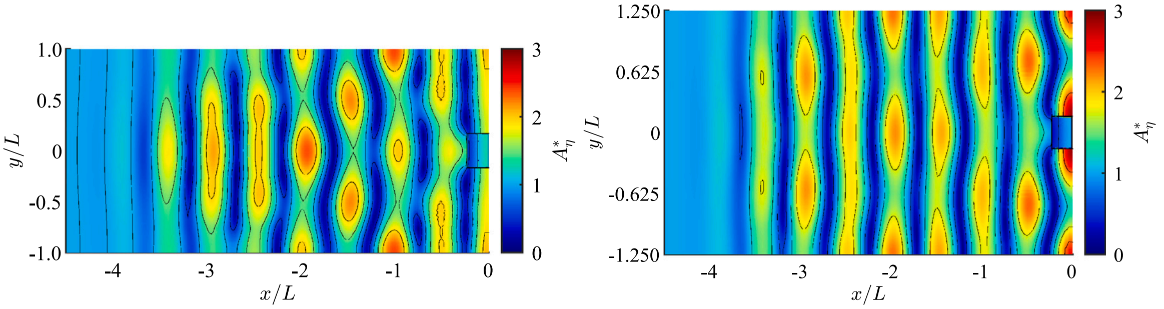

(a) A^*_η for $W/L = 2.00$ (b) A^*_η for $W/L = 2.50$

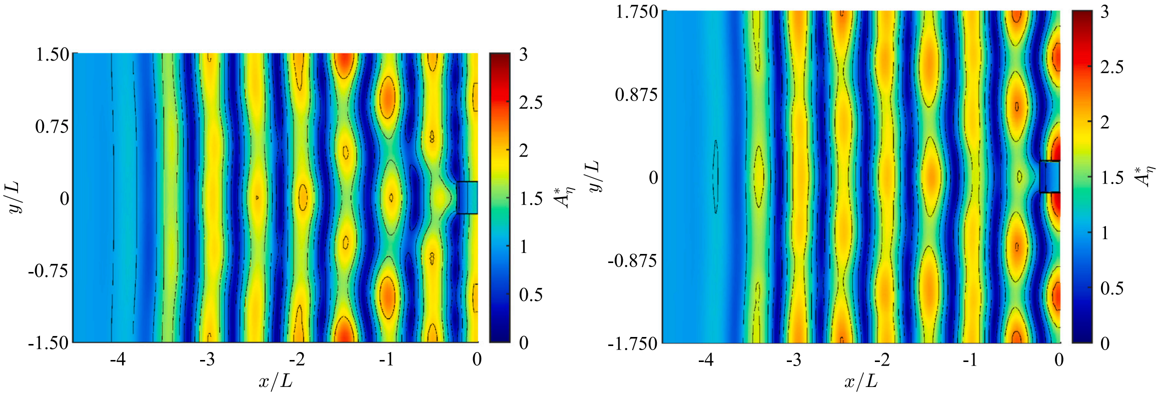

(c) A^*_η for $W/L = 3.00$ (d) A^*_η for $W/L = 3.50$.

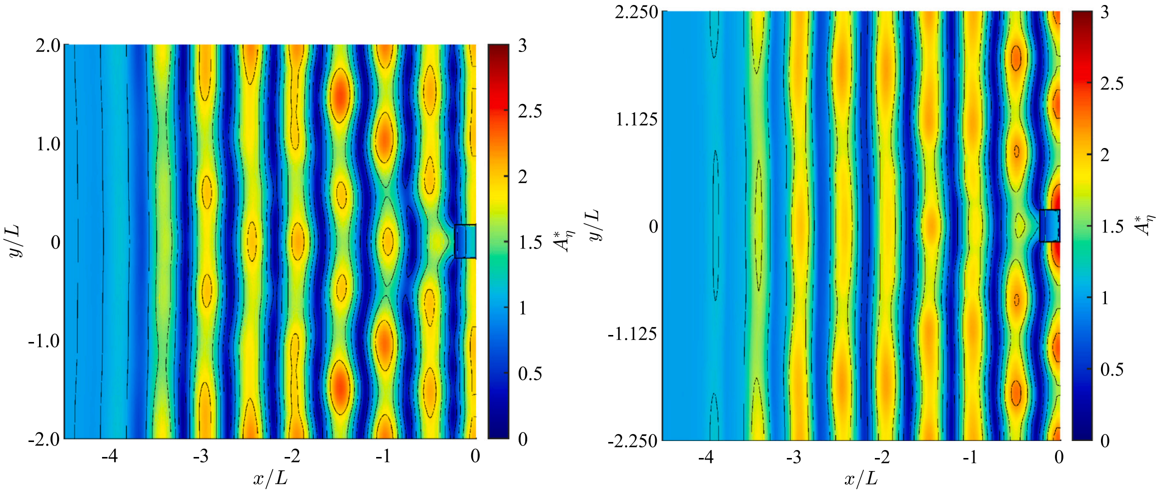

(e) A^*_η for $W/L = 4.00$. (f) A^*_η for $W/L = 4.50$.

Fig. 11. Non-dimensional wave height for $\frac{W}{L} = n$ and $\frac{W}{L} = n + \frac{1}{2}$ cases.

volume amplitude results (Figs. 9(a) to 9(c)), the energy transmission to the OWC is lower in these cases. This suggests that the higher local mean non-dimensional wave amplitude observed in the $W/L = n+3/4$ configurations arises primarily from wave reflections.

The local mean non-dimensional wave amplitude ($\bar{A}^*_\eta$) and the chamber dynamics of the OWC are interdependent, with wave amplitude influencing available energy for conversion, while the chamber response affects the surrounding wave field. The non-dimensional pressure amplitude ($A^*_{p_a}$), inherently linked to the energy density and wave amplitude, decreases as the energy density reduces. This reduction in pressure amplitude directly contributes to the observed decrease in system efficiency.

Similarly, the non-dimensional volume amplitude (A^*_V), which quantifies the oscillation of air volume within the chamber, is also sensitive to local wave dynamics. Lower wave amplitudes in front of the OWC lead to smaller air volume oscillations, further reducing the system's efficiency.

In wider flumes, the energy is distributed across a larger transverse area, leading to reduced local wave amplitudes, lower pressure oscillations, and diminished air volume oscillations. This reduction in local wave amplitudes, particularly pronounced in non-resonant configurations, also influences wave interference intensity (I) at the OWC opening and the spatial distribution of the reflected/scattered wave contribution, which will be discussed in the following section.

4.1.3. Implications for wave-OWC interaction

The reduction in local wave amplitudes in wider flumes directly impacts the efficiency of the OWC, as the energy density at the wave-structure interface is diminished. This explains the observed decrease in efficiency for non-optimal configurations, where energy is more

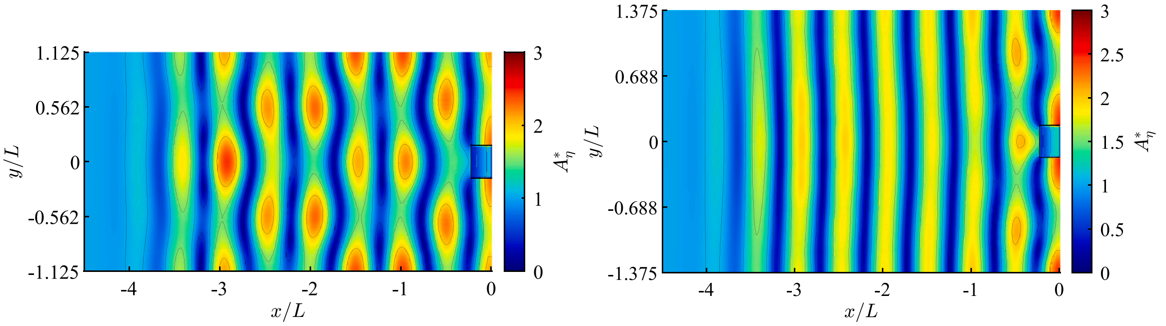

(a) A^*_η for $W/L = 2.25$

(b) A^*_η for $W/L = 2.75$

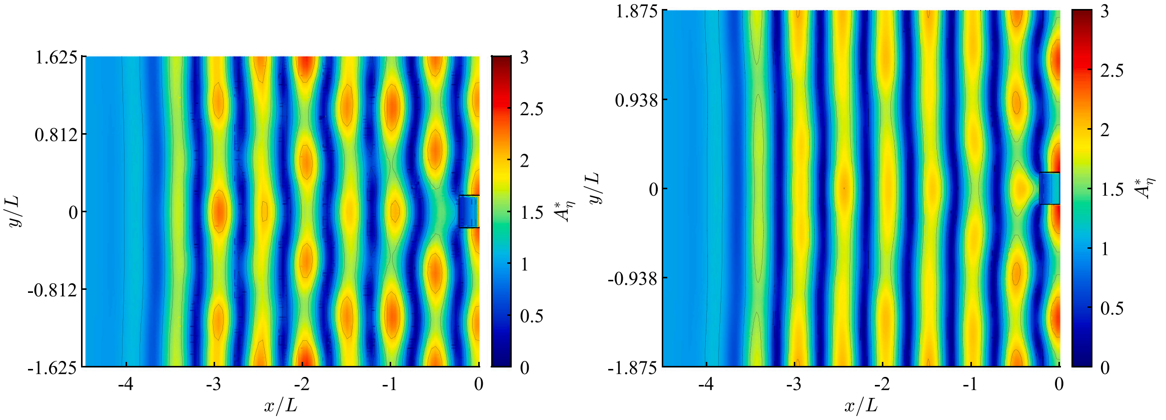

(c) A^*_η for $W/L = 3.25$

(d) A^*_η for $W/L = 3.75$.

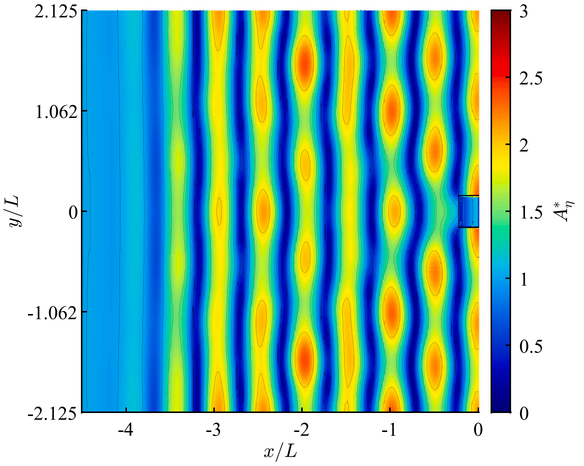

(e) A^*_η for $W/L = 4.25$.

Fig. 12. Non-dimensional wave height for $\frac{W}{L} = n + \frac{1}{4}$ and $\frac{W}{L} = n + \frac{3}{4}$ cases.

diffusely distributed across the flume rather than concentrated in front of the OWC.

The transverse standing waves also interact with the longitudinal wave field in the flume. When the resonance conditions in both dimensions align (e.g., integer values of W/L), the resulting constructive interference amplifies wave energy in front of the OWC, further enhancing efficiency. However, misalignment between transverse and longitudinal modes (e.g., at $W/L = n+1/2$) increases destructive interference, scattering wave energy and reducing energy capture efficiency. To better understand how wave interference intensity influences wave-OWC interactions and how the reflected/scattered wave contribution varies spatially, the next section quantifies their respective distributions and magnitudes.

4.2. Wave interference intensity and reflected/scattered wave contribution

To quantify the interaction between the reflected/scattered waves and the incident wave field at the OWC opening, the wave interference intensity was analysed along a line in the transverse direction (y) at the OWC opening.

The wave interference intensity along this line is defined as:

$$I(y) = A^*_{\eta_\Delta}(y) \cdot \cos(\Delta\phi(y)), \tag{23}$$

where:

- $A^*_{\eta_\Delta}(y)$ is the non-dimensional amplitude of the difference between the incident wave and the reflected/scattered wave at each position along the OWC opening.

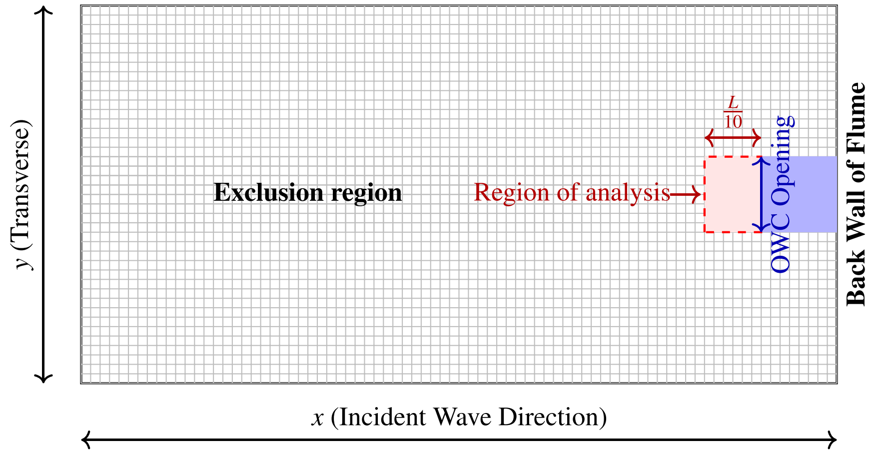

Fig. 13. Plan view of the land-fixed OWC and flume, highlighting the exclusion region and region of analysis.

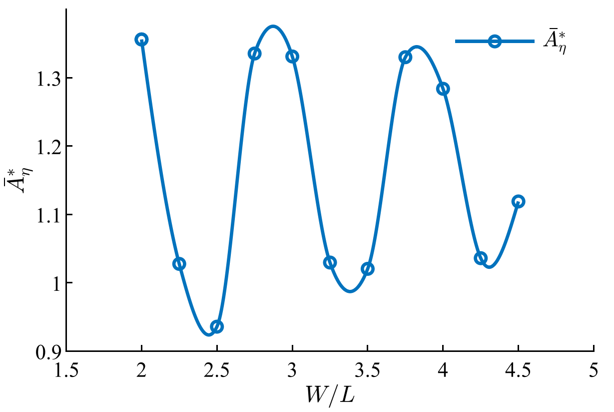

Fig. 14. Local mean non-dimensional wave amplitude ($\bar{A}^*_\eta$) for each case considered.

- $\Delta\phi(y)$ is the phase difference between the reflected/scattered waves and the incoming wave at each position along the OWC opening.
- $\cos(\Delta\phi(y))$ constrains the interference intensity between -1 and 1, where -1 indicates complete destructive interference, 1 indicates complete constructive interference, and intermediate values correspond to partial interference.

This formulation ensures that the interference intensity metric directly quantifies wave interactions where they are most significant, at the OWC opening. Since this method relies purely on temporal phase and amplitude variations at fixed locations, it is valid for standing wave conditions, where wave interference remains stationary over time. In addition to interference intensity, the reflected/scattered wave contribution metric (C_{η_R}) was introduced to analyse the spatial influence of reflected/scattered waves within the defined region of analysis.

The reflected/scattered wave contribution is defined as:

$$C_{\eta_R}(x,y) = A^*_{\eta_R}(x,y)\cdot\cos(\Delta\phi(x,y)), \tag{24}$$

where:

- $A^*_{\eta_R}(x,y)$ is the non-dimensional amplitude of the reflected/scattered wave field.
- $\Delta\phi(x,y)$ is the phase difference between the reflected/scattered waves and the incoming wave at each spatial location.
- $\cos(\Delta\phi(x,y))$ describes the phase relationship between the reflected/scattered and incident waves, ranging from -1 (completely out of phase, leading to destructive effects) to 1 (completely in phase, leading to constructive effects), with intermediate values representing partial contributions.

Unlike interference intensity, which is evaluated along a line at the OWC opening, the reflected/scattered wave contribution metric is evaluated over a localised region in front of the OWC opening, where the effects on efficiency are most pronounced. This approach captures the spatial influence of reflected and scattered waves within the analysis region, providing insight into their role in modifying the local wave field.

By evaluating interference intensity along a line and the reflected/scattered wave contribution over a localised region, we can assess both the wave interaction strength at the OWC opening and the localised influence of reflections and scattering on efficiency. The reflected/scattered wave field was isolated as:

$$\eta_R(x,y,t) = \eta(x,y,t) - \eta_0(x,y,t), \tag{25}$$

where the total wave surface $\eta(x,y,t)$ represents the combined incoming and reflected/scattered waves. The incident wave field η_0 follows the second-order Stokes wave formulation given in (14), accounting for both the primary wave component and the second-order correction due to nonlinear wave effects. To further analyse these waves, the incoming wave field and the reflected/scattered wave field were decomposed separately into their harmonic components:

$$\eta_i(x,y,t) = \sum_{n=1}^{\infty} A_{\eta_i,n}(x,y)\cos\left(n\Omega t + \phi_{i,n}(x,y)\right), \tag{26}$$

where i denotes either the incoming wave field ($i = 0$) or the reflected/scattered wave field ($i = R$). Here, $A_{\eta_i,n}(x,y)$ is the amplitude of the nth harmonic, Ω is the angular frequency of the fundamental harmonic (corresponding to the angular frequency of the incident wave), and $\phi_{i,n}(x,y)$ is the corresponding phase. Given the relatively minor contributions of higher-order harmonics, only the first harmonic is presented here for its relevance to the study. Phase wrapping was addressed by constraining $\Delta\phi(x,y)$ within $-\pi \le \Delta\phi(x,y) \le \pi$ using the following adjustment:

$$\Delta\phi(x,y) = \begin{cases} \Delta\phi(x,y) - 2\pi, & \text{if } \Delta\phi(x,y) > \pi, \\ \Delta\phi(x,y) + 2\pi, & \text{if } \Delta\phi(x,y) < -\pi. \end{cases} \tag{27}$$

This ensured phase differences remained within $-\pi$ to π, avoiding discontinuities. By taking the cosine of the phase difference ($\cos(\Delta\phi)$), values were constrained between -1 and 1, where 1 represents in-phase waves, 0 corresponds to a phase difference of $\pm\pi/2$, and -1 represents

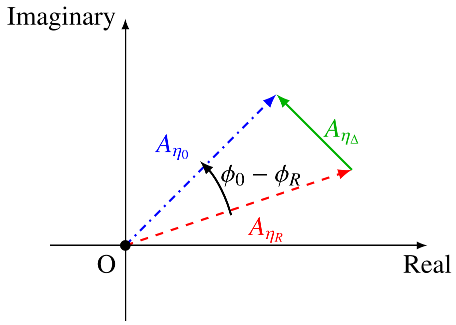

Fig. 15. Complex plane representation of the amplitude of the difference (A_{η_Δ}), illustrating the relationship between the incoming wave amplitude (A_{η_0}), reflected/scattered wave amplitude (A_{η_R}), and their phase difference ($\phi_0 - \phi_R$). The amplitude of the difference (A_{η_Δ}) corresponds to the magnitude of the complex difference between A_{η_0} and A_{η_R}, accounting for both amplitude and phase relations.

waves that are completely out of phase. Unlike purely phase-based measures, the wave interference intensity evaluated along a line at the OWC opening incorporates both the phase and wave amplitude differences. The use of $\cos(\Delta\phi)$ preserves the directional nature of the interference, distinguishing constructive interference ($\cos(\Delta\phi) > 0$) from destructive interference ($\cos(\Delta\phi) < 0$). Since the non-dimensional amplitude of the difference, $A^*_{\eta_\Delta}$, is unbounded, the wave interference intensity metric is similarly unrestricted in magnitude, fully capturing variations in wave amplitude. This formulation provides a more comprehensive representation of interference dynamics by accounting for phase alignment and amplitude variations. The amplitude of the difference (A_{η_Δ}) represents the magnitude of the complex difference between the incoming wave amplitude (A_{η_0}) and the reflected/scattered wave amplitude (A_{η_R}) in the complex plane (Fig. 15). This complex difference accounts for both the amplitudes and the relative phases of the two waves. It was calculated as:

$$A_{\eta_\Delta}(x,y) = \sqrt{A^2_{\eta_0}(x,y) + A^2_{\eta_R}(x,y) - 2A_{\eta_0}(x,y)A_{\eta_R}(x,y)\cos(\phi_0 - \phi_R)}, \tag{28}$$

where:

- $A_{\eta_0}(x,y)$ and $A_{\eta_R}(x,y)$ are the amplitudes of the incoming and reflected/scattered waves at position (x,y), respectively,
- ϕ_0 and ϕ_R are the phases of the incoming and reflected/scattered waves.

The non-dimensional amplitude of the difference was calculated as:

$$A^*_{\eta_\Delta}(x,y) = \frac{A_{\eta_\Delta}(x,y)}{A_0}, \tag{29}$$

where A_0 is the amplitude of the incident wave. Fig. 16 presents four illustrative cases of wave interference patterns to demonstrate the amplitude of the difference (A_{η_Δ}) between the incoming (A_{η_0}) and reflected/scattered (A_{η_R}) waves. In the case of constructive interference (Fig. 16(a)), the incoming and reflected/scattered waves are perfectly in phase ($\phi_0 = \phi_R$), resulting in maximum reinforcement and a resultant wave amplitude (A_η) equal to the sum of the individual amplitudes. Here, the amplitude of the difference (A_{η_Δ}) is zero because the peaks of the incoming and reflected/scattered waves align perfectly. Conversely, in the destructive interference case (Fig. 16(b)), the incoming and reflected/scattered waves are exactly out of phase ($\phi_0 - \phi_R = \pi$), leading to complete cancellation of the resultant wave amplitude. In this case, the amplitude of the difference is large, reflecting the complete separation between the peaks of the incoming and reflected/scattered waves. The second row of subfigures (Figs. 16(c) and 16(d)) illustrates scenarios where the incoming and reflected/scattered waves differ in both amplitude and phase. For in-phase waves with differing amplitudes (Fig. 16(c)), the resultant wave amplitude reflects the magnitude difference between the components, resulting in constructive interference. In this case, the amplitude of the difference is large because of the disparity in magnitudes between the incoming and reflected/scattered waves. For out-of-phase waves with differing amplitudes (Fig. 16(d)), the phase difference and amplitude disparity combine to produce partial destructive interference. Here, the amplitude of the difference is small because the wave components are closer in magnitude and the phase difference reduces the separation between peaks.

These examples are presented to demonstrate that the amplitude of the difference (A_{η_Δ}) alone does not directly indicate whether constructive or destructive interference is occurring. Rather, it quantifies the magnitude of the difference between the incoming and reflected/scattered wave fields, providing insight into the relative contributions of amplitude and phase differences to the overall interference pattern.

To visualise the spatial distribution of the extracted reflected/scattered wave field, Fig. 17 presents contour plots of the non-dimensional amplitude of the reflected/scattered waves $A^*_{\eta_R}$ for representative configurations of $W/L = n$ (Fig. 17(a)) and $W/L = n + 1/2$ (Fig. 17(b)). These figures highlight the regions where the reflected/scattered wave amplitudes are concentrated and provide insight into wave interaction mechanisms. In the integer width ratio case (Fig. 17(a)), the reflected/scattered wave amplitude exhibits a distinct peak in the near-field region, centrally aligned in the transverse direction and in line with the OWC opening, along with peaks in the transverse side regions. In contrast, the non-integer case (Fig. 17(b)) exhibits a greater reflected/scattered wave amplitude across the OWC opening and lacks the distinct central peak observed in the integer case. Instead, the peaks in the reflected/scattered wave amplitude appear more irregular in the near-field region and are more concentrated towards the transverse extents of the flume. Notably, this configuration also exhibits more pronounced peaks along the back wall and in the transverse side regions, with significant peaks on the exterior side walls of the OWC.

The spatial distribution of $\cos(\Delta\phi)$ is shown in Fig. 18 for representative cases of $W/L = n$ (Fig. 18(a)) and $W/L = n+1/2$ (Fig. 18(b)). In the integer width ratio case (Fig. 18(a)), the phase difference bands in the near-field and transverse side regions are notably less parallel, particularly at locations coincident with peaks in the reflected/scattered wave amplitude contours (Fig. 17). This suggests a spatial correlation between phase variation and the reflected/scattered wave amplitude. A similar trend is observed for the non-integer width ratio case (Fig. 18(b)), although the phase bands appear more structured and parallel in the near-field region, suggesting weaker transverse resonance effects. Notably, in the integer case (Fig. 18(a)), an in-phase band extends across the entire OWC opening, indicating a more uniform phase relationship in this region. In contrast, for the non-integer case (Fig. 18(b)), this band is significantly smaller and does not extend up to the OWC opening. Instead, a region of increased phase variation appears in front of the OWC, suggesting greater disruption in phase alignment between incident and reflected/scattered waves, which may reduce wave-structure interactions and alter energy transmission. These phase difference contours provide insight into the spatial coherence of wave interactions and serve as a precursor to the analysis of wave interference intensity at the OWC opening, as well as the spatial distribution of the reflected/scattered wave contribution.

The spatial distribution of $A^*_{\eta_\Delta}$ is depicted in Fig. 19 for selected cases of $W/L = n$ (Fig. 19(a)) and $W/L = n+1/2$ (Fig. 19(b)). This plot shares notable similarities with the non-dimensional amplitude of the reflected/scattered wave contours shown in Fig. 17 and, by extension, with the phase difference contours in Fig. 18, particularly in the near-field and transverse side regions. The peaks in $A^*_{\eta_\Delta}$ (Fig. 19) visually align with those in the reflected/scattered wave contours (Fig. 17), indicating a strong spatial correlation between regions of greater wave

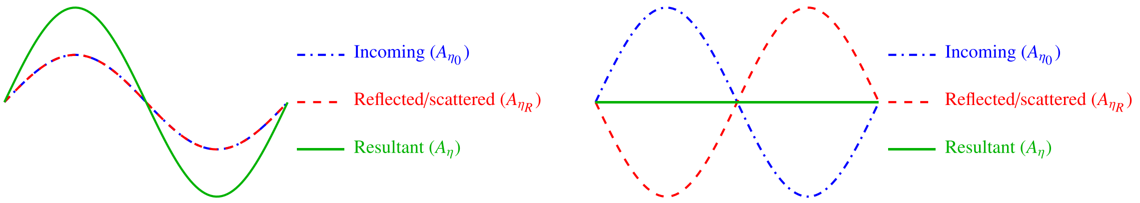

(a) Constructive interference with maximum resultant wave amplitude.

(b) Destructive interference resulting in cancellation.

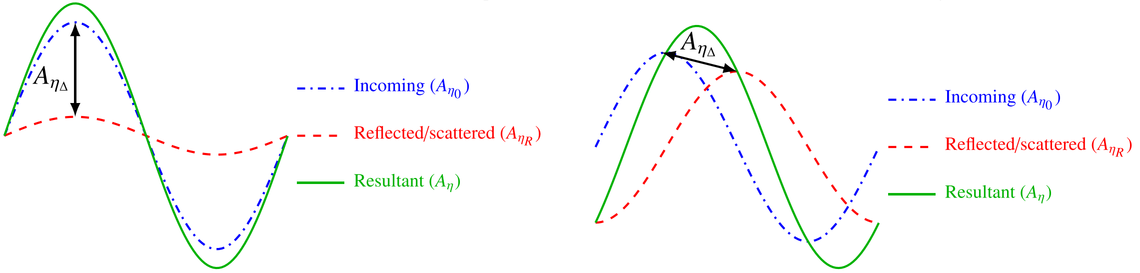

(c) In-phase waves with different amplitudes.

(d) Out-of-phase waves with differing amplitudes.

Fig. 16. Illustrations of wave interference patterns showing constructive and destructive interference, as well as cases of in-phase and out-of-phase waves with differing amplitudes.

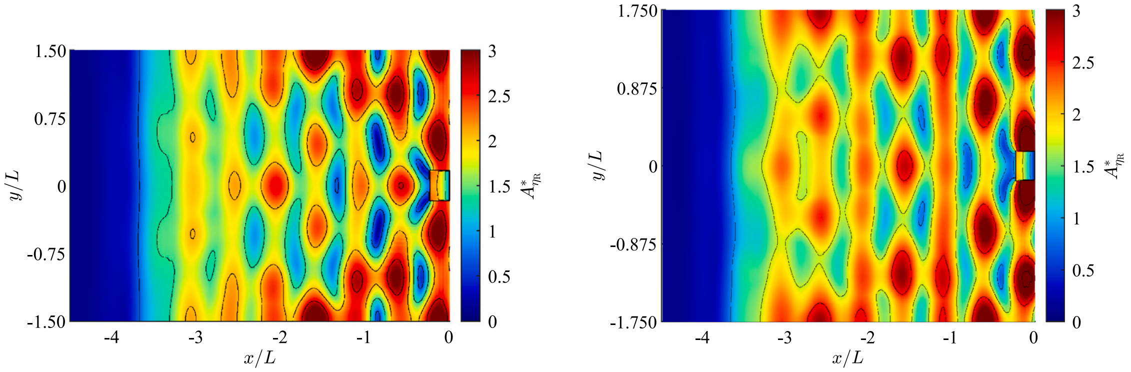

(a) Integer width ratio case $\frac{W}{L} = n$.

(b) Non-integer width ratio case $\frac{W}{L} = n + \frac{1}{2}$.

Fig. 17. Contour plots of the non-dimensional amplitude of the reflected/scattered waves $A^*_{\eta_R}$ for selected cases, where $n = 3$.

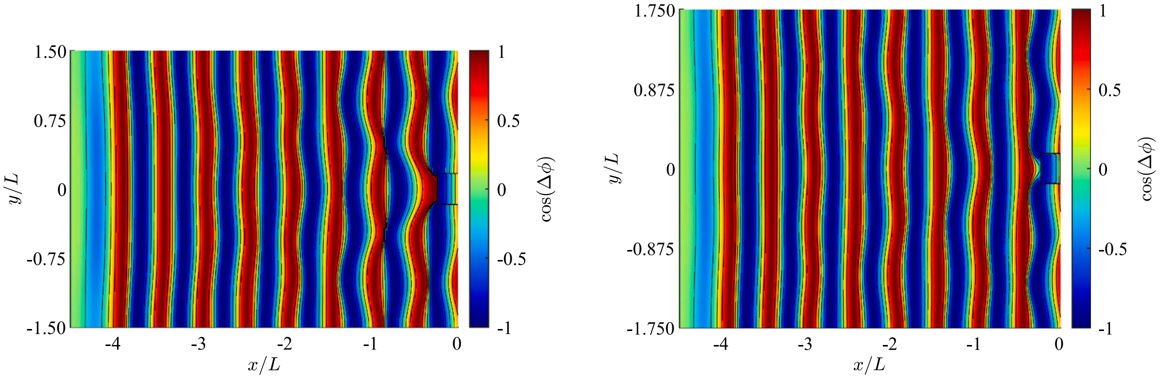

(a) Integer width ratio case $\frac{W}{L} = n$.

(b) Non-integer width ratio case $\frac{W}{L} = n + \frac{1}{2}$.

Fig. 18. Contour plots of $\cos(\Delta\phi)$, representing the phase relationship between the incident and reflected/scattered waves, for selected cases where $n = 3$.

amplitude difference and peaks in the reflected/scattered wave field. For the integer case (Fig. 19(a)), a distinct peak is observed in the near-field region in front of the OWC opening, highlighting a localised area where the incident and reflected/scattered waves differ significantly. Notably, directly at the OWC opening, the amplitude of the difference is smaller. In contrast, this distinct peak is absent in the non-integer case (Fig. 19(b)), where the amplitude of the difference is greater directly at the OWC opening compared to the integer case.

The spatial distribution of the normalised reflected/scattered wave contribution ($\tilde{C_{\eta_R}}$) for selected cases of $W/L = n$ and $W/L = n + 1/2$ is shown in Fig. 20. To facilitate a clearer comparison of reflected/scattered wave contribution patterns, the metric is normalised as:

$$\tilde{C_{\eta_R}}(x, y) = \frac{C_{\eta_R}(x, y)}{|C_{\eta_R}|_{\max}} \tag{30}$$

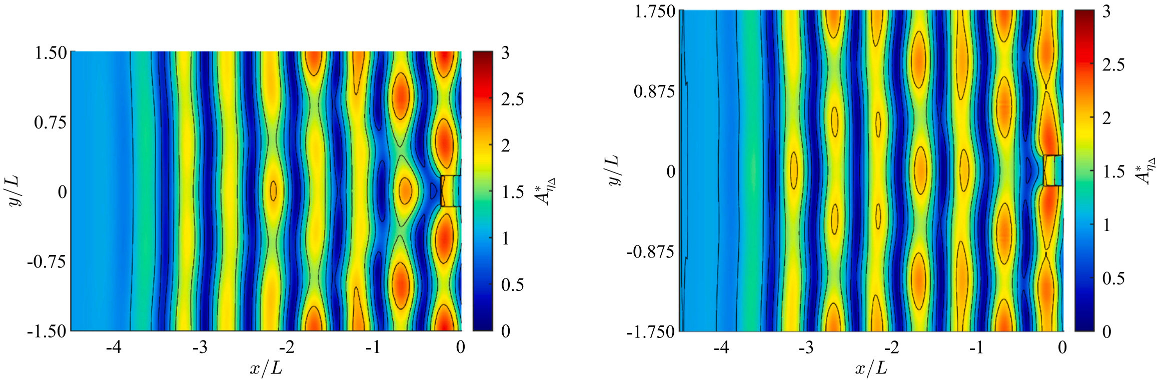

(a) Integer width ratio case $\frac{W}{L} = n$.

(b) Non-integer width ratio case $\frac{W}{L} = n + \frac{1}{2}$.

Fig. 19. Contour plots of the non-dimensional amplitude difference $A^*_{\eta_\Delta}$ for selected cases, where $n = 3$.

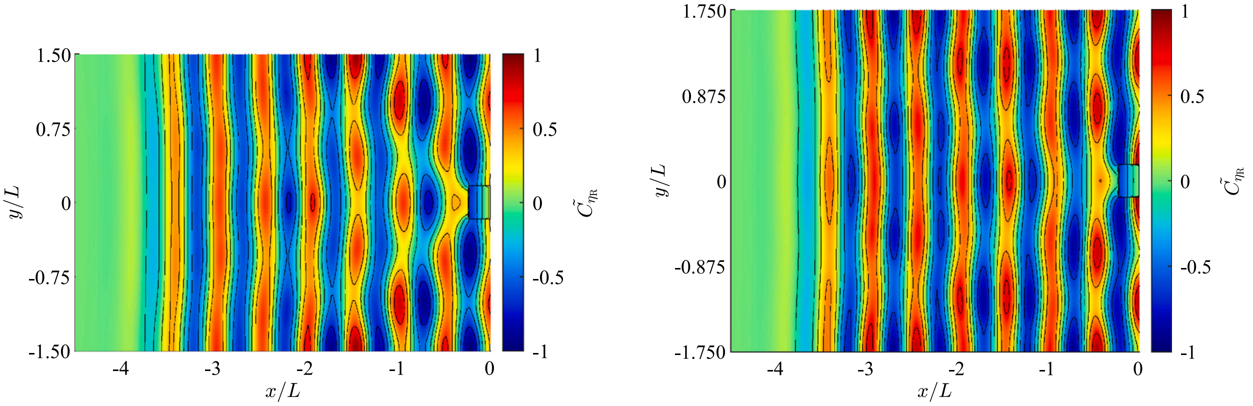

(a) Integer width ratio case $\frac{W}{L} = n$.

(b) Non-integer width ratio case $\frac{W}{L} = n + \frac{1}{2}$.

Fig. 20. Contour plots of the normalised reflected/scattered wave contribution $\tilde{C_{\eta_R}}$ for selected cases, where $n = 3$.

where $|C_{\eta_R}|_{\max}$ denotes the maximum absolute value of $C_{\eta_R}(x, y)$ within the domain. Normalisation enhances the visibility of reflected/scattered wave contribution patterns but removes information about absolute magnitudes, making these plots most useful for identifying spatial distributions rather than for direct quantitative comparisons.

In these plots, positive values correspond to regions where constructive contributions dominate, while negative values indicate regions of destructive contributions. This distinction provides a clearer representation of how reflected/scattered wave contributions vary spatially within the domain.

Both cases exhibit strong similarities with the $\cos(\Delta\phi)$ plots shown in Fig. 18. In the integer width ratio case (Fig. 20(a)), constructive contributions are more pronounced in the near-field region, particularly at the OWC opening, where the entire width is covered by a region of constructive contribution. In contrast, in the non-integer width ratio case (Fig. 20(b)), regions of destructive contributions encroach into the near-field region, especially at the extents of the OWC opening, where the transition between the transverse side regions and near-field occurs. However, the non-integer case also exhibits greater constructive contributions on the leeward side of the OWC opening in the transverse side regions, suggesting a redistribution of wave energy in this configuration.

Additionally, peaks of both constructive and destructive contributions are more defined in the integer case. In contrast, they appear more diffuse in the non-integer case, both in the near-field and transverse side regions. This suggests that transverse resonance is more pronounced in the integer case than in the non-integer case.

4.2.1. *Mean local wave interference intensity and reflected/scattered wave contribution*

The mean local wave interference intensity was calculated as:

$$\bar{I} = \frac{1}{W_{OWC}} \int_{W_{OWC}} I(y)\,\mathrm{d}y, \tag{31}$$

where:

- W_{OWC} is the length of the line at the OWC opening,
- $I(y)$ is the wave interference intensity at each position along the line.

The mean local reflected/scattered wave contribution was calculated as:

$$\bar{C}_{\eta_R} = \frac{1}{A} \int_{A} C_{\eta_R}(x, y)\,\mathrm{d}A, \tag{32}$$

where:

- A is the area of the defined region,
- $C_{\eta_R}(x, y)$ is the reflected/scattered wave contribution at each spatial location.

The variation in mean local wave interference intensity and mean local reflected/scattered wave contribution with changes in W/L is illustrated in Fig. 21.

The results show that the mean local wave interference intensity is positive for integer width ratio cases ($W/L = n$), indicating that constructive interference dominates. This corresponds to greater

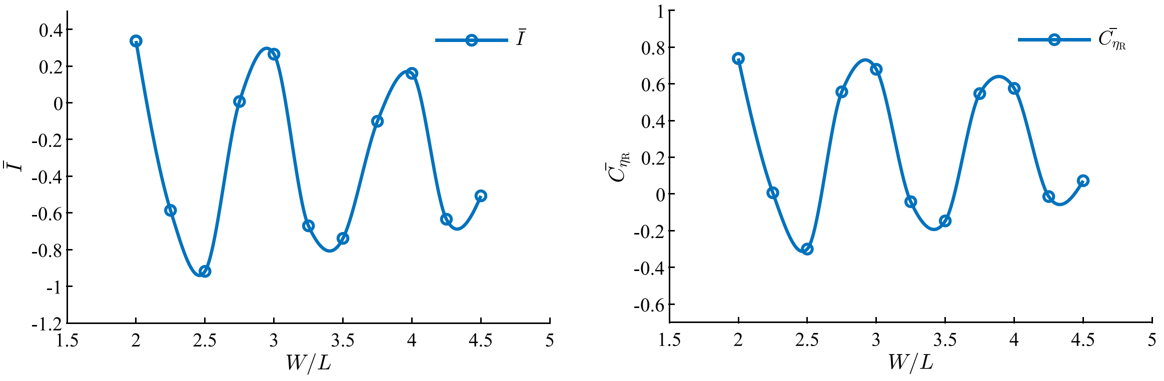

(a) Mean local wave interference intensity $\bar{I}$.

(b) Mean local reflected/scattered wave contribution $\bar{C}_{\eta_{\mathrm{R}}}$.

Fig. 21. Mean local wave interference intensity and mean local reflected/scattered wave contribution.

constructive reflected/scattered wave contributions and stronger wave-structure interactions, leading to higher efficiency in these cases. For three-quarter integer cases ($W/L = n + 3/4$), the interference intensity is negative; however, the magnitude of destructive interference is significantly lower than in the other non-integer cases. In particular, for ($W/L = n+1/4$) and ($W/L = n+1/2$), the mean local wave interference intensity is negative with a much greater magnitude, indicating that destructive interference is dominant. This trend correlates with the spatial distribution of the reflected/scattered wave contribution, which exhibits stronger amplitudes in the near-field region, particularly at the OWC opening and at the extent of the OWC opening for non-integer cases. The greater destructive contributions in these regions suggest increased scattering effects, which could contribute to the observed suppression of constructive interference at the OWC opening.

A similar trend is observed in the mean local reflected/scattered wave contribution ($\bar{C}_{\eta_{\mathrm{R}},1}$), reinforcing the relationship between wave reflection effects and interference patterns. The similarity in their trends suggests that wave interference intensity at the OWC opening is closely tied to the broader spatial distribution of reflected/scattered waves.

A key trend in both metrics is their decreasing magnitude with increasing flume width. This behaviour mirrors the mean local wave amplitude, suggesting that as the flume becomes wider, interference and reflection effects weaken, approaching an equilibrium point beyond which further increases in width have minimal impact. Notably, the magnitude of destructive interference in non-integer cases decreases at a greater rate than the decrease in constructive interference in integer cases. This indicates that as the flume widens, destructive interference effects are increasingly suppressed, whereas constructive interference persists more consistently, albeit at lower intensity.

For the range of flume widths examined in this study, the magnitude of destructive interference is initially greater than constructive interference for smaller widths. However, as the flume width increases, this imbalance diminishes, with the magnitude of destructive interference decreasing more rapidly relative to the magnitude of constructive interference. This suggests that within this range, transverse resonance effects, which enhance constructive interference in integer cases, remain more resilient to increasing flume width than the destructive interference effects observed in non-integer cases.

The alignment between the trends in wave interference intensity and the reflected/scattered wave contribution further supports the hypothesis that interference intensity at the OWC opening is primarily governed by the strength and spatial distribution of the reflected wave field. Future studies could explore how these interactions evolve under different wave conditions or alternative OWC configurations, with more refined spatial analysis methods to further resolve wave interference patterns.

5. Conclusion

This study examined the influence of flume width on the performance of a land-fixed OWC wave energy converter, focusing on how wave interactions and resonance conditions affect efficiency. Using a validated numerical model, simulations were conducted for a range of width-to-wavelength ratios (W/L) to evaluate their impact on wave dynamics and energy conversion. The results demonstrated that integer width ratios ($W/L = n$) lead to well-defined wave interaction patterns, with enhanced wave amplification in front of the OWC opening, resulting in higher efficiency. In contrast, non-integer width ratios ($W/L = n + 1/2$) exhibited disrupted resonance conditions, with greater wave cancellation effects encroaching into the near-field region, particularly at the extents of the OWC opening, leading to reduced efficiency.

These findings have implications beyond the flume environment, particularly for the spacing of multiple OWCs along a shoreline. The observed dependence of wave interaction patterns on transverse resonance conditions suggests that OWC performance may be optimised by carefully selecting device placement to align with constructive wave zones. Conversely, suboptimal spacing could increase wave cancellation effects, limiting energy extraction.

To further characterise wave interactions in front of the OWC, this study introduced the reflected/scattered wave contribution metric, which captured the influence of the reflected and scattered waves on the local wave field. The results showed that the reflected/scattered wave contribution follows a similar trend to the interference intensity at the OWC opening, reinforcing the connection between wave reflection effects and energy conversion efficiency. By evaluating the reflected/scattered wave contribution over a localised region in front of the OWC, this metric provided insight into how wave reflections influence energy availability in the near-field region, particularly in non-integer width ratio cases.

Although this study considered a single incident wave period, this choice represents the prevailing wave period for a given shoreline location. In addition, this study employed idealised flume geometry and regular wave conditions to isolate the influence of the width-to-wavelength ratio. While this approach allows for systematic analysis of geometric resonance effects, it does not capture the complexity of real coastal environments, such as variable bathymetry or broadband sea states. As such, the applicability of the observed trends to real-world settings should be considered within the context of these simplifications. The extent to which the observed trends generalise to real-world conditions remains an open question, requiring further study across a broader range of wave climates and OWC configurations.

Future work could extend this analysis by investigating the influence of additional parameters, such as incident wave conditions, chamber geometry, or turbine characteristics, to determine whether the observed trends persist across different configurations. In particular, the effect of oblique wave incidence on transverse resonance and interference patterns warrants investigation, as does the performance of multi-OWC arrays placed within confined domains. Furthermore, more refined spatial analysis methods could help resolve directional wave interactions more explicitly, improving our understanding of how reflected and scattered waves propagate within the domain. By further refining the relationship between wave interaction patterns and OWC efficiency, this approach could contribute to optimising OWC array placement along shorelines for enhanced wave energy capture.

CRediT authorship contribution statement

Heath Palmer: Writing – original draft, Visualization, Validation, Investigation, Formal analysis, Data curation. **Ming Zhao:** Writing – review & editing, Supervision, Software, Resources, Methodology, Conceptualization. **Helen Wu:** Writing – review & editing, Supervision. **Pan Hu:** Writing – review & editing, Supervision. **Adnan Munir:** Writing – review & editing. **Zhang Qin:** Writing – review & editing, Resources. **Vatsal Dhamelia:** Writing – review & editing.

Declaration of competing interest

The authors declare that they have no known competing financial interests or personal relationships that could have appeared to influence the work reported in this paper.

References

[1] C. Wang, Y. Zhang, Performance enhancement for a dual-chamber OWC conceived from side wall effects in narrow flumes, Ocean Eng. 247 (2022) Cited by: 11.

[2] R. Muduli, S.B. Patil, D. Karmakar, Hydrodynamic performance of pile restrained u-shaped OWC device using boundary element method, Eng. Anal. Bound. Elem. 158 (2024) 139–159.

[3] S. Razavi, R. Shafaghat, B.A. Kharkeshi, J. Eskandari, 3D numerical modeling and geometry optimization of an Oscillating Water Column device in sloshing conditions using openfoam and genetic algorithms, J. Appl. Fluid Mech. (2024).

[4] M. Peymani, A.H. Nikseresht, H.B. Bingham, A 3d numerical investigation of the influence of the geometrical parameters of an i-beam attenuator OWC on its performance at the resonance period, Energy 286 (2024).

[5] C. Xu, Y. He, Y. Yao, J. Zuo, Experimental and numerical study of a circular OWC with a u-shaped duct for wave energy conversion in long waves: Hydrodynamic characteristics and viscous energy loss, Renew. Energy 215 (2023).

[6] Y. Sun, D. Ning, R. Mayon, Q. Chen, Experimental and numerical investigation on hydrodynamic performance of a 3d land-fixed OWC wave energy converter, Appl. Ocean Res. 141 (2023) 103805.

[7] E. Didier, P.R. Teixeira, Numerical analysis of 3d hydrodynamics and performance of an array of Oscillating Water Column wave energy converters integrated into a vertical breakwater, Renew. Energy 225 (2024) 120297.

[8] A.A. Medina Rodríguez, R. Silva Casarín, J.M. Blanco Ilzarbe, A 3d boundary element method for analysing the hydrodynamic performance of a land-fixed Oscillating Water Column device, Eng. Anal. Bound. Elem. 138 (2022) 407–422.

[9] Y. Goda, Y. Suzuki, Estimation of Incident and Reflected Waves in Random Wave Experiment, Vol. 1976-July, 1977, pp. 828–845.

[10] S. Zhu, Separation of regular waves by a transfer function method, Ocean Eng. (1999).

[11] K.D. Suh, W.S. Park, B.S. Park, Separation of incident and reflected waves in wave–current flumes, Coast. Eng. 43 (2001) 149–159.

[12] C.-Y. Lin, C.-J. Huang, Decomposition of incident and reflected higher harmonic waves using four wave gauges, Coast. Eng. 51 (2004) 395–406.

[13] M.R. Eldrup, T.L. Andersen, Estimation of incident and reflected wave trains in highly nonlinear two-dimensional irregular waves, J. Waterw. Port Coast. Ocean. Eng. 145 (2019) 04018038.

[14] I. Herdayanditya, E. Lataire, P. Rauwoens, Spatial variations in numerical wave tanks with active wave generating–absorbing system, Ocean Eng. 315 (2025).

[15] Y. Wei, T. Abadie, A. Henry, F. Dias, Wave interaction with an oscillating wave surge converter. part ii: Slamming, Ocean Eng. 113 (2016) 319–334.

[16] X. Zhao, Q. Zou, J. Geng, Y. Zhang, Z. Wang, Influences of wave resonance on hydrodynamic efficiency and loading of an OWC array under oblique waves, Appl. Ocean Res. 120 (2022) Cited by: 27.

[17] X. Zhao, Y. Li, Q. Zou, D. Han, J. Geng, Long wave absorption by a dual purpose helmholtz resonance OWC breakwater, Coast. Eng. 178 (2022) Cited by: 24.

[18] M. Zhao, H. Palmer, V. Dhamelia, H. Wu, Three-dimensional numerical simulation of a cylindrical Oscillating Water Column (OWC) device placed in a wave flume, Renew. Energy 231 (2024) 120930.

[19] N.G. Jacobsen, D.R. Fuhrman, J. Fredsøe, A wave generation toolbox for the open-source cfd library: Openfoam®, Internat. J. Numer. Methods Fluids 70 (2012) 1073–1088.

[20] M. Zhao, B. Teng, L. Cheng, A new form of generalized boussinesq equations for varying water depth, Ocean Eng. 31 (2004) 2047–2072.

[21] C. Josset, A.H. Clément, A time-domain numerical simulator for Oscillating Water Column wave power plants, Renew. Energy 32 (2007) 1379–1402.

[22] P.R.F. Teixeira, D.P. Davyt, E. Didier, R. Ramalhais, Numerical simulation of an Oscillating Water Column device using a code based on navier–stokes equations, Energy 61 (2013) 513–530.

[23] R.A.A.C. Gonçalves, P.R.F. Teixeira, E. Didier, F.R. Torres, Numerical analysis of the influence of air compressibility effects on an Oscillating Water Column wave energy converter chamber, Renew. Energy 153 (2020) 1183–1193.

[24] W. Sheng, A. Lewis, Wave energy conversion of Oscillating Water Column devices including air compressibility, J. Renew. Sustain. Energy 8 (2016).

[25] M.R. Mia, M. Zhao, H. Wu, A. Munir, Numerical investigation of scaling effect in two-dimensional Oscillating Water Column wave energy devices for harvesting wave energy, Renew. Energy 178 (2021) 1381–1397.

[26] A. Viviano, R.E. Musumeci, D. Vicinanza, E. Foti, Pressures induced by regular waves on a large scale OWC, Coast. Eng. 152 (2019).

[27] L. Ciappi, L. Cheli, I. Simonetti, A. Bianchini, G. Manfrida, L. Cappietti, Wave-to-wire model of an oscillating-water-column wave energy converter and its application to mediterranean energy hot-spots, Energies 13 (2020) Cited by: 27; All Open Access, Gold Open Access, Green Open Access.

[28] L. Ciappi, I. Simonetti, A. Bianchini, L. Cappietti, G. Manfrida, Application of integrated wave-to-wire modelling for the preliminary design of Oscillating Water Column systems for installations in moderate wave climates, Renew. Energy 194 (2022) 232–248.

[29] J. Henriques, J. Portillo, W. Sheng, L. Gato, A. Falcão, Dynamics and control of air turbines in oscillating-water-column wave energy converters: Analyses and case study, Renew. Sustain. Energy Rev. 112 (2019) 571–589.

[30] R.Q. Wang, D.Z. Ning, C.W. Zhang, Q.P. Zou, Z. Liu, Nonlinear and viscous effects on the hydrodynamic performance of a fixed OWC wave energy converter, Coast. Eng. 131 (2018) 42–50.

[31] A. Brito-Melo, L. Gato, A. Sarmento, Analysis of wells turbine design parameters by numerical simulation of the OWC performance, Ocean Eng. 29 (2002) 1463–1477.